




Article

Crystal Structure, Spectroscopic Investigations, and Physical Properties of the Ternary Intermetallic $REPt_2Al_3$ ($RE = Y, Dy-Tm$) and $RE_2Pt_3Al_4$ Representatives ($RE = Tm, Lu$)

Fabian Eustermann¹, Simon Gausebeck¹, Carsten Dosche², Mareike Haensch² ,
Gunther Wittstock²  and Oliver Janka^{1,2,*} 

¹ Institut für Anorganische und Analytische Chemie, Universität Münster, Corrensstrasse 30, 48149 Münster, Germany; f_eust01@wwu.de (F.E.); simongausebeck@gmx.de (S.G.)

² Institut für Chemie, Carl von Ossietzky Universität Oldenburg, 26111 Oldenburg, Germany; carsten.dosche@uni-oldenburg.de (C.D.); mareike.haensch@uni-oldenburg.de (M.H.); gunther.wittstock@uni-oldenburg.de (G.W.)

* Correspondence: ocjanka@uni-muenster.de; Tel.: +49-251-83-36074

Received: 1 March 2018; Accepted: 10 April 2018; Published: 16 April 2018



Abstract: The $REPt_2Al_3$ compounds of the late rare-earth metals ($RE = Y, Dy-Tm$) were found to crystallize isostructural. Single-crystal X-ray investigations of YPt_2Al_3 revealed an orthorhombic unit cell ($a = 1080.73(6)$, $b = 1871.96(9)$, $c = 413.04(2)$ pm, $wR2 = 0.0780$, 942 F^2 values, 46 variables) with space group $Cmmm$ ($oC48$; q^2pji^2hedb). A comparison with the Pearson database indicated that YPt_2Al_3 forms a new structure type, in which the Pt and Al atoms form a $[Pt_2Al_3]^{\delta-}$ polyanion and the Y atoms reside in the cavities within the framework. Via a group-subgroup scheme, the relationship between the $PrNi_2Al_3$ -type structure and the new YPt_2Al_3 -type structure was illustrated. The compounds with $RE = Dy-Tm$ were characterized by powder X-ray diffraction experiments. While YPt_2Al_3 is a Pauli-paramagnet, the other $REPt_2Al_3$ ($RE = Dy-Tm$) compounds exhibit paramagnetic behavior, which is in line with the rare-earth atoms being in the trivalent oxidation state. $DyPt_2Al_3$ and $TmPt_2Al_3$ exhibit ferromagnetic ordering at $T_C = 10.8(1)$ and $4.7(1)$ K and $HoPt_2Al_3$ antiferromagnetic ordering at $T_N = 5.5(1)$ K, respectively. Attempts to synthesize the isostructural lutetium compound resulted in the formation of $Lu_2Pt_3Al_4$ ($Ce_2Ir_3Sb_4$ -type, $Pnma$, $a = 1343.4(2)$, $b = 416.41(8)$, $c = 1141.1(2)$ pm), which could also be realized with thulium. The structure was refined from single-crystal data ($wR2 = 0.0940$, 1605 F^2 values, 56 variables). Again, a polyanion with bonding Pt–Al interactions was found, and the two distinct Lu atoms were residing in the cavities of the $[Pt_3Al_4]^{\delta-}$ framework. X-ray photoelectron spectroscopy (XPS) measurements were conducted to examine the electron transfer from the rare-earth atoms onto the polyanionic framework.

Keywords: intermetallics; crystal structure; group-subgroup; magnetic properties; XPS

1. Introduction

In the field of intermetallic compounds [1,2], some structure types are found with an impressive number of entries listed in the Pearson database [3]. Amongst them are the binary Laves phases of the $MgCu_2$ -type ($Fd\bar{3}m$) [4] and $MgZn_2$ -type ($P6_3/mmc$) [5] structures (together with more than 5500 entries), the cubic Cu_3Au -type ($Pm\bar{3}m$, >1950 entries) structures [6], and the hexagonal $CaCu_5$ -type ($P6/mmm$, >1650 entries) structures [7]. For ternary intermetallic compounds, the tetragonal body-centered $ThCr_2Si_2$ -type ($I4/mmm$, >3250 entries) [8], the orthorhombic $TiNiSi$ -type ($Pnma$, >1550 entries), and the hexagonal $ZrNiAl$ -type ($P6_2m$, >1450 entries) [9] representatives show a

broad variety of compounds with numerous, different elemental combinations. The structures and physical properties of the equiatomic $RETX$ (RE = rare-earth element, T = transition metal, X = element of group 12–15) representatives have been recently summarized in a series of review articles [10–13].

Derived from the binary $CaCu_5$ -type structure, two prototypic ternary representatives with different chemical compositions have been reported: the $CeCo_3B_2$ - [14] and the $PrNi_2Al_3$ -type [15] structures. From a crystal chemical point of view, YNi_2Al_3 is also worth mentioning [16], because this compound can be considered to be an i3-superstructure of the $PrNi_2Al_3$ -type structure. Recently, an i7-superstructure of $PrNi_2Al_3$ has also been reported, which was also found for $ErPd_2Al_3$ [17]. Our interests in the compounds of the $REPt_2Al_3$ series originate from the fact that only $CePt_2Al_3$ ($PrNi_2Al_3$ -type) has been reported previously [18]. Therefore, we synthesized and characterized the missing members of the $REPt_2Al_3$ series with the late, small rare-earth elements. From a basic research point of view, investigations of the magnetic ground state of the open f -shell rare-earth atoms are also of great interest.

2. Experimental

2.1. Synthesis

The starting materials for the synthesis of the $REPt_2Al_3$ and $RE_2Pt_3Al_4$ samples were pieces of the sublimed rare-earth elements (Y, Dy–Tm, and Lu from Smart Elements), platinum sheets (Agosi), and aluminum turnings (Koch Chemicals), all with stated purities better than 99.9%. For the $REPt_2Al_3$ compounds (RE = Y, Dy–Tm), the elements were weighed in the ideal 1:2:3 atomic ratio and arc-melted [19] in a water-cooled copper hearth under 800 mbar of argon pressure. The argon gas was purified with a titanium sponge (873 K), molecular sieves, and silica gel. Re-melting of the obtained buttons from each site several times enhanced the homogeneity. The as-cast buttons of the yttrium compound were crushed, and the fragments were sealed in quartz ampoules, placed in the water-cooled sample chamber of a high-frequency furnace (Typ TIG 5/300, Hüttinger Elektronik, Freiburg, Germany) [20], and heated until a softening of the piece was observed. The power was subsequently reduced by 10%, and the sample was kept at this temperature for 120 min before being cooled to room temperature. The other samples were annealed in muffle furnaces. They were heated to 1223 K and then kept at this temperature for 14 days, followed by slow cooling until they reached 573 K. Afterwards, the furnace was switched off. These different annealing procedures led to X-ray pure samples suitable for physical properties measurements. For the $RE_2Pt_3Al_4$ compounds (RE = Tm, Lu), the elements were weighed in the ideal 2:3:4 atomic ratio and arc-melted as described above. Again, an annealing step in a high-frequency furnace was subsequently conducted. The specimens are stable in air over weeks and show metallic luster; the ground samples are grey.

2.2. X-ray Image Plate Data and Data Collections

The polycrystalline samples were characterized at room temperature by powder X-ray diffraction on a Guinier camera (equipped with an image plate system, Fujifilm, Nakanuma, Japan, BAS-1800,) using $Cu K\alpha_1$ radiation and α -quartz ($a = 491.30$, $c = 540.46$ pm, Riedel-de-Haën, Seelze, Germany) as an internal standard. The lattice parameters (Table 1) were obtained from a least-squares fit. Proper indexing of the diffraction lines was ensured by an intensity calculation [21].

Irregularly shaped crystal fragments of the YPt_2Al_3 and $Lu_2Pt_3Al_4$ compounds were obtained from the annealed crushed buttons. The crystals were glued to quartz fibers using beeswax, and their quality was checked by Laue photographs on a Buerger camera (white molybdenum radiation, image plate technique, Fujifilm, Nakanuma, Japan, BAS-1800) for intensity data collection. The datasets were collected on a Stoe StadiVari four-circle diffractometer (Mo- $K\alpha$ radiation ($\lambda = 71.073$ pm); μ -source; oscillation mode; hybrid-pixel-sensor, Dectris Pilatus 100 K [22]) with an open Eulerian cradle setup. Numerical absorption correction along with scaling was applied to the datasets. All relevant crystallographic data, deposition, and details of the data collection and

evaluation are listed in Tables 2–8. Further details of the crystal structure investigation may be obtained from the Fachinformationszentrum Karlsruhe, 76344 Eggenstein-Leopoldshafen, Germany (Fax: +49-7247-808-666; E-Mail: crysdata@fiz-karlsruhe.de, http://www.fiz-karlsruhe.de/request_for_deposited_data.html) by quoting the depository numbers CSD-434174 (YPt₂Al₃) and CSD-434175 (Lu₂Pt₃Al₄).

2.3. Energy Dispersive X-ray Spectroscopy (EDX) Data

The crystals measured on the diffractometer were analyzed semi-quantitatively using a Zeiss EVO MA10 scanning electron microscope with YF₃, TmF₃, LuF₃, Pt, and Al₂O₃ as standards. No impurity elements heavier than sodium (the detection limit of the instrument) were observed. The experimentally determined element ratios (YPt₂Al₃: 18 ± 2 at.% Y: 29 ± 2 at.% Pt: 53 ± 2 at.% Al; and Lu₂Pt₃Al₄: 20 ± 2 at.% Y: 36 ± 2 at.% Pt: 44 ± 2 at.% Al) were in close agreement with the ideal compositions (16.7:33.3:50 and 22.2:33.3:44.5), respectively. The deviations resulted from the irregular shape of the crystal surfaces (conchoidal fracture). Additionally, polycrystalline pieces from the annealed arc-melted buttons were embedded in a methymethacrylate matrix and polished with diamond and SiO₂ emulsions of different particle sizes. During the first attempts to synthesize TmPt₂Al₃ and LuPt₂Al₃, phase segregation was observed; the secondary phases had the compositions Tm₂Pt₃Al₄ and Lu₂Pt₃Al₄.

2.4. Magnetic Properties Measurements

Fragments of the annealed buttons of the X-ray pure REPt₂Al₃ phases were attached to the sample holder rod of a vibrating sample magnetometer (VSM) unit using Kapton foil for measuring the magnetization $M(T, H)$ in a Quantum Design physical property measurement system (PPMS). The samples were investigated in the temperature range of 2.5–300 K with external magnetic fields up to 80 kOe. The magnetic data are summarized in Table 9.

2.5. X-ray Photoelectron Spectroscopy (XPS)

XPS was performed using an ESCALAB 250 Xi instrument (Thermo Fisher, East Grinstead, UK) with mono-chromatized Al K α ($h\nu = 1486.6$ eV) radiation. All samples were cleaned by Ar⁺ sputtering (MAGCIS ion gun, 36 keV) for 60 s to remove adventitious carbon. High-resolution spectra were measured with pass energies of 10 eV (Pt 4f, Al 2s, Al 2p, and C 1s) and 20 eV (Y 3d and Pr 3d). Peak deconvolution was performed using a Gaussian-Lorentzian peak shape by the software Advantage (Thermo Fisher). All spectra were referenced to remaining adventitious carbon at 284.8 eV. Because of the overlap of the Pt 4f and Al 2p signals, Al 2s was used for Al quantification. The obtained data are summarized in Table 10.

3. Results and Discussion

During attempts to synthesize aluminum intermetallics with the composition REPt₂Al₃, well-resolved X-ray powder patterns for the small rare-earth elements RE = Y, Dy–Tm were observed. For the thulium compound, additional reflections showed up in the unannealed sample, which were initially interpreted as impurities. Subsequently, single crystals from the yttrium sample were isolated and structurally investigated (*vide infra*). The large and early rare-earth elements (RE = La–Nd, Sm, Gd, and Tb) do not form the same structure type. Investigations on the structures formed by these elements are still ongoing. Attempts to synthesize LuPt₂Al₃ also yielded a diffraction pattern different from the slightly larger rare-earth elements Dy–Tm. As cast specimen, TmPt₂Al₃ and LuPt₂Al₃ were subsequently investigated by scanning electron microscopy coupled with energy dispersive X-ray spectroscopy (SEM/EDX). The impurity phase in TmPt₂Al₃ and the main phase in nominal LuPt₂Al₃ were found to be Tm₂Pt₃Al₄ and Lu₂Pt₃Al₄, respectively. Finally, samples with these compositions were prepared, and single crystals from Lu₂Pt₃Al₄ were isolated and investigated.

3.1. Structure Refinements

A careful analysis of the obtained intensity dataset of YPt_2Al_3 revealed an orthorhombic C-centered lattice. The centrosymmetric group $Cmmm$ was found to be correct during structure refinement. A systematic check of the Pearson database [3], using Pearson code $oC48$ and Wyckoff sequence q^2pji^2hedb , gave no matches; hence, YPt_2Al_3 must be considered a new structure type. The starting atomic parameters were obtained using SuperFlip [23], implemented in Jana2006 [24,25]. The structure was refined on F^2 with anisotropic displacement parameters for all atoms. As a check for the correct composition and site assignment, the occupancy parameters were refined in a separate series of least-squares cycles. All sites were fully occupied within three standard deviations. No significant residual peaks were evident in the final difference Fourier syntheses. At the end, the positional parameters were transformed to the setting required for the group-subgroup scheme discussed below. Figure 1 depicts the X-ray powder diffraction pattern of YPt_2Al_3 along with the calculated pattern obtained using the positional information from the single-crystal structure refinement.

$\text{Lu}_2\text{Pt}_3\text{Al}_4$ was also found to crystallize in the orthorhombic crystal system with space group $Pnma$. A comparison with the Pearson database [3], using Pearson code $oP36$ and Wyckoff sequence c^9 , indicated isotypism with $\text{Ce}_2\text{Ir}_3\text{Sb}_4$ [26,27]. The structure was refined on F^2 with anisotropic displacement parameters for all atoms. As a check for the correct composition and site assignment, the occupancy parameters were refined in a separate series of least-squares cycles. All sites were fully occupied within three standard deviations. No significant residual peaks were evident in the final difference Fourier syntheses. In the powder X-ray diffraction experiments, trace amounts of TmPtAl or LuPtAl (TiNiSi-type) were evident. Thermal treatment was not able to remove these impurities. The details of the structure refinement, final positional parameters, and interatomic distances are listed in Tables 2–8.

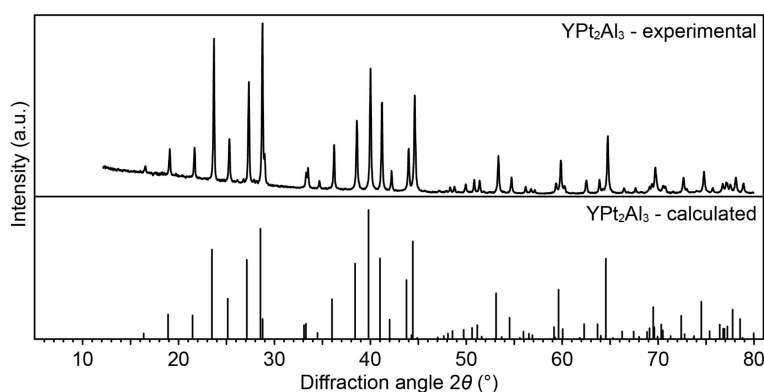


Figure 1. Experimental (top) and calculated (bottom) Guinier powder pattern ($\text{CuK}\alpha_1$ radiation) of YPt_2Al_3 .

Table 1. Lattice parameters of the orthorhombic REPt_2Al_3 series (YPt_2Al_3 -type, rare-earth (RE) = Y, Dy–Tm), space group $Cmmm$, and $\text{RE}_2\text{Pt}_3\text{Al}_4$ series ($\text{Ce}_2\text{Ir}_3\text{Sb}_4$ -type, RE = Y, Dy–Tm), space group $Pnma$.

| Compound | <i>a</i> (pm) | <i>b</i> (pm) | <i>c</i> (pm) | <i>V</i> (nm ³) |
|-------------------------------------|---------------|---------------|---------------|-----------------------------|
| YPt_2Al_3 | 1080.73(6) | 1871.96(9) | 413.04(2) | 0.8356 |
| DyPt_2Al_3 | 1081.3(1) | 1872.7(2) | 413.93(5) | 0.8382 |
| HoPt_2Al_3 | 1079.26(4) | 1869.46(6) | 413.55(2) | 0.8344 |
| ErPt_2Al_3 | 1077.31(6) | 1866.0(1) | 413.14(4) | 0.8305 |
| TmPt_2Al_3 | 1075.38(9) | 1862.6(1) | 412.87(4) | 0.8270 |
| $\text{Tm}_2\text{Pt}_3\text{Al}_4$ | 1349.9(3) | 418.22(8) | 1143.7(2) | 0.6429 |
| $\text{Lu}_2\text{Pt}_3\text{Al}_4$ | 1343.4(2) | 416.41(8) | 1141.1(2) | 0.6383 |

Table 2. Crystallographic data and structure refinement for YPt₂Al₃, space group *Cmmm*, *Z* = 8, own type and Lu₂Pt₃Al₄, space group *Pnma*, *Z* = 4, Ce₂Ir₃Sb₄-type.

| Compound | YPt ₂ Al ₃ | Lu ₂ Pt ₃ Al ₄ |
|---|----------------------------------|---|
| Molar mass, g mol ^{−1} | 560.0 | 1043.1 |
| Density calc., g cm ^{−3} | 8.93 | 10.91 |
| Crystal size, μm | 25 × 40 × 55 | 30 × 30 × 40 |
| Detector distance, mm | 40 | 40 |
| Exposure time, s | 25 | 50 |
| Integr. param. A, B, EMS | 6.2; −5.2; 0.017 | 5.0; −4.1; 0.012 |
| Range in <i>hkl</i> | ±16; ±28, ±6 | ±21; ±6, ±18 |
| θ_{\min} , θ_{\max} , deg | 2.2–32.9 | 2.3–35.5 |
| Linear absorption coeff., mm ^{−1} | 81.2 | 97.0 |
| No. of reflections | 11,714 | 21,601 |
| $R_{\text{int}}/R_{\sigma}$ | 0.1124/0.0178 | 0.1411/0.1152 |
| No. of independent reflections | 942 | 1605 |
| Reflections used [$I \geq 3\sigma(I)$] | 795 | 679 |
| $F(000)$, e | 1872 | 1712 |
| $R1/wR2$ for $I \geq 3\sigma(I)$ | 0.0341/0.0770 | 0.0415/0.0798 |
| $R1/wR2$ for all data | 0.0422/0.0780 | 0.1095/0.0940 |
| Data/parameters | 942/46 | 1605/56 |
| Goodness-of-fit on F^2 | 2.22 | 1.23 |
| Extinction coefficient | 161(17) | 73(6) |
| Diff. Fourier residues/e [−] Å ^{−3} | −4.15/3.97 | −4.98/4.51 |

Table 3. Atom positions and equivalent isotropic displacement parameters (pm²) for YPt₂Al₃. U_{eq} is defined as one-third of the trace of the orthogonalized U_{ij} tensor.

| Atom | Wyckoff | <i>x</i> | <i>y</i> | <i>z</i> | U_{eq} |
|----------|------------|------------|------------|----------|-----------------|
| Position | | | | | |
| Y1 | 2 <i>d</i> | 0 | 0 | 1/2 | 151(7) |
| Y2 | 4 <i>e</i> | 1/4 | 1/4 | 0 | 137(4) |
| Y3 | 2 <i>b</i> | 1/2 | 0 | 0 | 137(6) |
| Pt1 | 4 <i>h</i> | 0.27855(6) | 0 | 1/2 | 120(2) |
| Pt2 | 8 <i>q</i> | 0.13928(4) | 0.13927(3) | 1/2 | 120(1) |
| Pt3 | 4 <i>i</i> | 0 | 0.33333(4) | 0 | 136(2) |
| Al1 | 4 <i>j</i> | 0 | 0.2483(3) | 1/2 | 128(14) |
| Al2 | 8 <i>q</i> | 0.3729(4) | 0.1244(2) | 1/2 | 138(10) |
| Al3 | 8 <i>p</i> | 0.2244(4) | 0.0748(2) | 0 | 160(11) |
| Al4 | 4 <i>i</i> | 0 | 0.1494(4) | 0 | 157(16) |

Table 4. Atom positions and equivalent isotropic displacement parameters (pm²) for Lu₂Pt₃Al₄. U_{eq} is defined as one-third of the trace of the orthogonalized U_{ij} tensor. $y = 1/4$ all 4*c*.

| Atom | <i>x</i> | <i>z</i> | U_{eq} |
|------|-------------|-------------|-----------------|
| Lu1 | 0.01840(10) | 0.71349(12) | 199(3) |
| Lu2 | 0.29143(10) | 0.57858(14) | 218(3) |
| Pt1 | 0.13365(9) | 0.24522(11) | 196(3) |
| Pt2 | 0.38024(9) | 0.06876(11) | 201(3) |
| Pt3 | 0.62220(9) | 0.58482(11) | 189(3) |
| Al1 | 0.0017(7) | 0.0827(9) | 210(2) |
| Al2 | 0.0714(8) | 0.4553(8) | 180(20) |
| Al3 | 0.3017(7) | 0.8651(9) | 190(30) |
| Al4 | 0.3174(7) | 0.2828(9) | 170(20) |

Table 5. Anisotropic displacement parameters (pm^2) for YPt_2Al_3 . Coefficients U_{ij} of the anisotropic displacement factor tensor of the atoms are defined by: $-2\pi^2[(ha^*)^2U_{11} + \dots + 2hka^*b^*U_{12}]$. $U_{13} = U_{23} = 0$.

| Atom | U_{11} | U_{22} | U_{33} | U_{12} |
|------|----------|----------|----------|----------|
| Y1 | 144(10) | 139(11) | 169(14) | 0 |
| Y2 | 137(7) | 137(7) | 136(9) | −1(6) |
| Y3 | 135(10) | 140(10) | 136(12) | 0 |
| Pt1 | 126(3) | 122(3) | 112(3) | 0 |
| Pt2 | 117(2) | 131(2) | 112(3) | 7(1) |
| Pt3 | 147(3) | 153(3) | 107(4) | 0 |
| Al1 | 160(2) | 120(20) | 110(30) | 0 |
| Al2 | 138(16) | 145(17) | 130(20) | −18(14) |
| Al3 | 210(20) | 156(18) | 110(20) | 40(15) |
| Al4 | 110(20) | 220(30) | 140(30) | 0 |

Table 6. Anisotropic displacement parameters (pm^2) for $\text{Lu}_2\text{Pt}_3\text{Al}_4$. Coefficients U_{ij} of the anisotropic displacement factor tensor of the atoms are defined by: $-2\pi^2[(ha^*)^2U_{11} + \dots + 2hka^*b^*U_{12}]$. $U_{13} = U_{23} = 0$.

| Atom | U_{11} | U_{22} | U_{33} | U_{12} |
|------|----------|----------|----------|----------|
| Lu1 | 194(5) | 209(6) | 194(5) | −4(4) |
| Lu2 | 234(6) | 228(6) | 191(5) | −5(5) |
| Pt1 | 192(5) | 206(6) | 190(5) | −14(4) |
| Pt2 | 215(5) | 203(5) | 183(5) | −15(4) |
| Pt3 | 179(5) | 204(5) | 184(4) | −9(4) |
| Al1 | 200(40) | 220(40) | 210(40) | 10(4) |
| Al2 | 280(50) | 130(40) | 120(30) | 30(3) |
| Al3 | 120(40) | 210(50) | 240(50) | 0 |
| Al4 | 200(40) | 130(40) | 170(40) | 20(3) |

Table 7. Interatomic distances (pm) for YPt_2Al_3 . All distances of the first coordination spheres are listed. All standard uncertainties were less than 0.2 pm.

| | | | | | | | | | | | |
|------|---|-----|-------|------|---|-----|-------|------|---|-----|-------|
| Y1: | 2 | Pt1 | 300.7 | Pt2: | 1 | Al1 | 253.3 | Al2: | 1 | Pt2 | 253.7 |
| | 4 | Pt2 | 300.7 | | 1 | Al2 | 253.7 | | 1 | Pt1 | 253.7 |
| | 4 | Al4 | 347.3 | | 2 | Al4 | 256.0 | | 2 | Pt3 | 260.1 |
| | 8 | Al3 | 347.6 | | 2 | Al3 | 256.0 | | 1 | Al2 | 274.4 |
| | | | | | 1 | Pt1 | 300.7 | | 1 | Al1 | 274.8 |
| Y2: | 2 | Pt3 | 311.7 | Pt3: | 1 | Y1 | 300.7 | Al3: | 2 | Al3 | 277.3 |
| | 4 | Pt2 | 315.8 | | 1 | Pt2 | 300.7 | | 2 | Y2 | 339.6 |
| | 2 | Al3 | 328.8 | | 1 | Y2 | 315.8 | | 2 | Y3 | 339.9 |
| | 2 | Al4 | 329.0 | | 4 | Al2 | 260.1 | | 2 | Pt2 | 256.0 |
| | 4 | Al2 | 339.6 | | 2 | Al1 | 260.5 | | 2 | Pt1 | 256.0 |
| | 4 | Al1 | 339.7 | | 2 | Y2 | 311.7 | | 2 | Al2 | 277.3 |
| Y3: | 2 | Pt3 | 311.7 | Al1: | 1 | Y3 | 311.7 | Al4: | 1 | Al4 | 279.6 |
| | 4 | Pt2 | 315.8 | | 2 | Al3 | 343.6 | | 1 | Al3 | 279.7 |
| | 2 | Al3 | 328.8 | | 1 | Al4 | 343.9 | | 1 | Y3 | 328.8 |
| | 2 | Al4 | 329.0 | | 1 | Y2 | 311.7 | | 1 | Y2 | 328.8 |
| | 4 | Al2 | 339.6 | | 2 | Pt2 | 253.3 | | 1 | Pt3 | 343.6 |
| | 4 | Al1 | 339.7 | | 2 | Pt3 | 260.5 | | 2 | Y1 | 347.6 |
| | | | | | 2 | Al2 | 274.8 | | | | |
| Pt1: | 2 | Al2 | 253.9 | Al4: | 4 | Pt2 | 256.0 | | | | |
| | 4 | Al3 | 256.0 | | 2 | Y2 | 339.7 | | 2 | Al1 | 277.1 |
| | 2 | Pt2 | 300.7 | | 2 | Al3 | 279.6 | | 2 | Al3 | 279.6 |
| | 1 | Y1 | 300.7 | | 2 | Y2 | 329.0 | | 2 | Y2 | 329.0 |
| | 2 | Y3 | 315.8 | | 1 | Pt3 | 343.9 | | 1 | Pt3 | 343.9 |
| | | | | | 2 | Y1 | 347.6 | | 2 | Y1 | 347.6 |

Table 8. Interatomic distances (pm) for Lu₂Pt₃Al₄. All distances of the first coordination spheres are listed. All standard uncertainties were less than 0.2 pm.

| | | | | | | | | | | | |
|------|---|-----|-------|------|---|-----|-------|------|---|-----|-------|
| Lu1: | 2 | Pt3 | 298.8 | Pt2: | 2 | Al2 | 253.1 | Al2: | 2 | Pt2 | 253.1 |
| | 2 | Pt1 | 302.0 | | 1 | Al4 | 254.9 | | 1 | Pt3 | 253.6 |
| | 2 | Pt2 | 310.4 | | 1 | Al2 | 258.1 | | 1 | Pt2 | 258.1 |
| | 1 | Al4 | 326.8 | | 1 | Al1 | 258.1 | | 2 | Al4 | 287.6 |
| | 1 | Al2 | 327.1 | | 2 | Lu2 | 298.0 | | 1 | Lu2 | 302.7 |
| | 1 | Al3 | 336.8 | | 2 | Lu1 | 310.4 | | 2 | Lu2 | 307.6 |
| | 1 | Al1 | 338.9 | | | | | | 1 | Lu1 | 327.1 |
| | 2 | Al4 | 343.4 | Pt3: | 1 | Al1 | 250.3 | | | | |
| | 2 | Al1 | 344.4 | | 1 | Al2 | 253.5 | Al3: | 1 | Pt1 | 250.2 |
| | 2 | Al3 | 346.8 | | 1 | Al3 | 256.3 | | 1 | Pt3 | 256.3 |
| | | | | | 2 | Al4 | 266.3 | | 2 | Pt1 | 266.0 |
| Lu2: | 1 | Pt1 | 268.8 | | 2 | Lu2 | 294.9 | | 2 | Al3 | 280.5 |
| | 2 | Pt3 | 294.9 | | 2 | Lu1 | 298.8 | | 1 | Al1 | 291.0 |
| | 2 | Pt2 | 298.0 | | | | | | 2 | Lu2 | 312.7 |
| | 1 | Al2 | 302.7 | Al1: | 1 | Pt3 | 250.3 | | 1 | Lu1 | 336.8 |
| | 1 | Al4 | 304.4 | | 1 | Pt2 | 258.1 | | 2 | Lu1 | 346.8 |
| | 2 | Al2 | 307.6 | | 2 | Pt1 | 269.1 | | | | |
| | 2 | Al3 | 312.7 | | 1 | Al4 | 278.3 | Al4: | 1 | Pt1 | 247.6 |
| | 2 | Al1 | 312.9 | | 1 | Al3 | 291.0 | | 1 | Pt2 | 254.9 |
| | | | | | 2 | Lu2 | 312.9 | | 2 | Pt3 | 263.3 |
| Pt1: | 1 | Al4 | 247.6 | | 1 | Lu1 | 338.9 | | 2 | Al1 | 278.3 |
| | 1 | Al3 | 250.2 | | 2 | Lu1 | 344.4 | | 2 | Al2 | 287.6 |
| | 2 | Al3 | 266.0 | | | | | | 1 | Lu2 | 304.4 |
| | 1 | Lu2 | 268.8 | | | | | | 2 | Lu1 | 326.8 |
| | 2 | Al1 | 269.1 | | | | | | 1 | Lu1 | 343.4 |
| | 2 | Lu1 | 302.0 | | | | | | | | |

Table 9. Magnetic properties of the YPt₂Al₃-type compounds. T_N , Néel temperature; T_C , Curie temperature; μ_{eff} , effective magnetic moment; μ_{calc} , calculated magnetic moment; θ_p , paramagnetic Curie temperature; μ_{sat} , saturation moment; and saturation according to $g_J \times J$. The experimental saturation magnetizations were obtained at 3 K and 80 kOe.

| | T_N (K) | T_C (K) | μ_{eff} (μ_B) | μ_{calc} (μ_B) | θ_p (K) | μ_{sat} (μ_B) | $g_J \times J$ (μ_B) |
|-----------------------------------|-----------|-----------|--|---------------------------------|----------------|--------------------------------|----------------------------|
| YPt ₂ Al ₃ | | | Pauli-paramagnetic $\chi(300 \text{ K}) = 1.85(1) \times 10^{-4} \text{ emu mol}^{-1}$ | | | | |
| DyPt ₂ Al ₃ | – | 10.8(1) | 10.67(1) | 10.65 | +1.0(1) | 5.54(1) | 10 |
| HoPt ₂ Al ₃ | 5.5(1) | – | 10.59(1) | 10.61 | +2.0(1) | 7.23(1) | 10 |
| ErPt ₂ Al ₃ | – | – | 9.77(1) | 9.58 | +4.0(1) | 6.26(1) | 9 |
| TmPt ₂ Al ₃ | – | 4.7(1) | 7.69(1) | 7.56 | +12.8(1) | 4.25(1) | 7 |

3.2. The YPt₂Al₃-Type Structure: Crystal Chemistry and Group-Subgroup Relations

The isostructural aluminum compounds of the REPt₂Al₃ series (RE = Y, Dy–Tm) crystallize in the orthorhombic crystal system, space group *Cmmm*, Pearson code *oC48* and Wyckoff sequence $q^2 p j i^2 h e d b$. The lattice parameters (Figure 2) and unit cell volumes (Table 1) decrease from the dysprosium to the thulium compound, as expected, from the lanthanide contraction. The lattice parameters of the yttrium compound are in the same range, explainable by the similar ionic radii (Y³⁺: 90 pm; Dy³⁺: 91 pm; Ho³⁺: 90 pm [28]).

As YPt₂Al₃ was investigated by single-crystal X-ray diffraction experiments, its crystal structure will be used for the structural discussion. A view of the crystal structure along the crystallographic *c* axis is depicted in Figure 3. The crystal structure features a polyanionic [Pt₂Al₃]^{δ−} network and shows full Pt/Al ordering. The heteroatomic Pt–Al distance range from 253 to 261 pm indicates substantial Pt–Al bonding, because these distances are in the range of the sum of the covalent radii for Pt+Al

of $129 + 125 = 254$ pm [29]. The polyanionic networks of YPtAl (TiNiSi-type) [30] and $\text{Y}_4\text{Pt}_9\text{Al}_{24}$ ($\text{Y}_4\text{Pt}_9\text{Al}_{24}$ -type) [31] show similar distances of 257–269 and 246–274 pm, respectively. Additionally, homoatomic Al–Al distances ranging from 274 to 280 pm, and Pt–Pt distances of 301 pm can be found. The latter distances are slightly longer compared to what is found in elemental Pt (Cu-type, 284 pm) [32], while the aluminum distances are in line with elemental Al (Cu-type, 286 pm) [33]. Three crystallographically distinct Y^{3+} cations can be found in the cavities of the polyanion. They exhibit 18-fold coordination environments in the shape of six-fold-capped hexagonal prisms (Figure 4). The hexagonal prisms have slightly different compositions of $\text{Y1@}[\text{Al}_{12}+\text{Pt}_6]$, $\text{Y2@}[\text{Al}_8\text{Pt}_4+\text{Al}_4\text{Pt}_2]$, and $\text{Y3@}[\text{Al}_8\text{Pt}_4+\text{Al}_4\text{Pt}_2]$. The Y–Pt distances range from 301 to 316 pm; the Y–Al distances are 329 pm. While the former distances are in line with YPtAl, the latter distances are significantly longer (Y–Pt: 304–320 pm; Y–Al: 287–305 pm) [30].

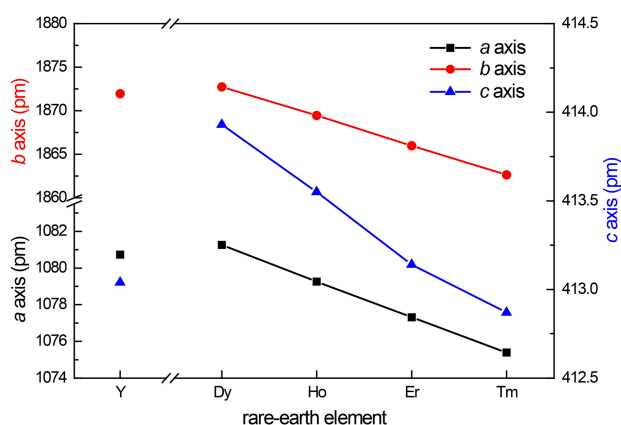


Figure 2. Plot of the unit cell parameters of the REPt_2Al_3 phases as a function of the rare-earth element.

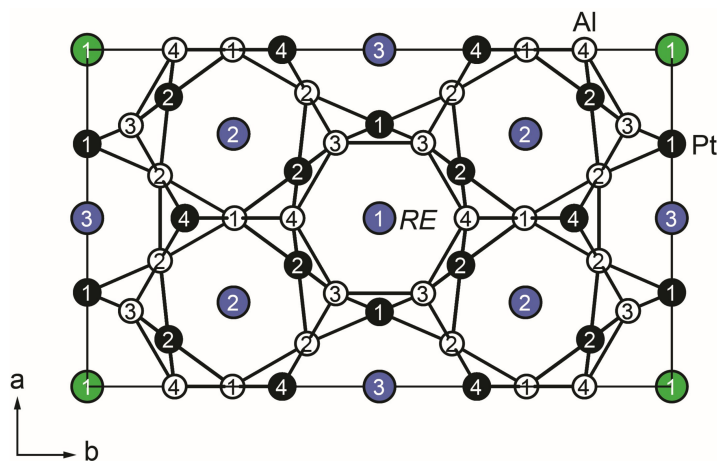


Figure 3. The crystal structure of YPt_2Al_3 . Yttrium, platinum, and aluminum atoms are drawn as green/blue, black-filled, and open circles, respectively. The polyanionic $[\text{Pt}_2\text{Al}_3]^\delta-$ network is highlighted.

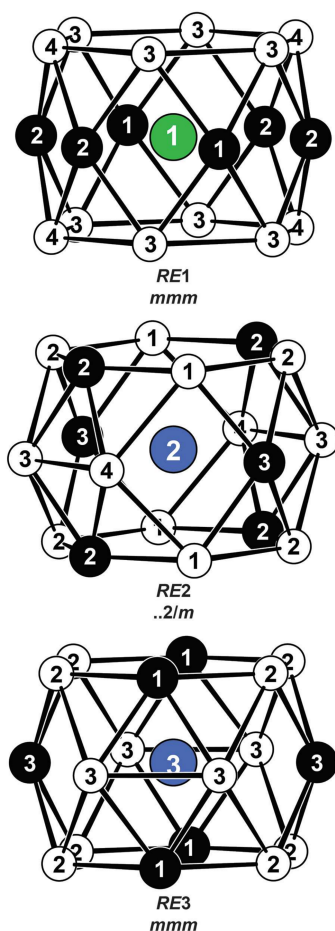


Figure 4. Coordination polyhedra surrounding the three crystallographically independent yttrium sites in YPt_2Al_3 . Yttrium, platinum, and aluminum atoms are drawn as green/blue, black-filled, and open circles, respectively. The local site symmetries are given.

A view of the unit cell along the c axis readily reminds us of the ternary CaCu_5 -type derivatives PrNi_2Al_3 [15], YNi_2Al_3 [16], DyNi_4Si [34], CeCo_3B_2 [14], and the recently found $i7$ superstructure of PrNi_2Al_3 [17]. Recoloring in intermetallics is found quite frequently, often accompanied by distortions and puckering within the respective structures [35]. These structural effects between different structure types can be investigated by so-called group-subgroup relations. The structures of PrNi_2Al_3 and YPt_2Al_3 are related by such a group-subgroup scheme, which is presented in the *Bärnighausen* formalism [36–39] in Figure 5. In the first step, an isomorphic symmetry reduction of index 4 takes place, which causes a doubling of the a and b axis, along with a splitting of the Pr ($1a$ to $1a$ and $3f$), Ni ($2c$ to $2c$ and $6l$), and Al ($3g$ to $6k$ and $6m$) sites. In the second step a *translationengleiche* transition of index 3 takes place, reducing the hexagonal symmetry from space group $P6/mmm$ to orthorhombic $Cmmm$. Again, a splitting of the crystallographic position occurs along with the introduction of additional degrees of freedom regarding the crystallographic positions. This enables a distortion of the polyanion and a recoloring of the crystallographic sites. The Y1 atoms finally occupy the $2d$ rather than the $2a$ site as suggested by the group-subgroup scheme. Hence, they are shifted by $1/2 z$ compared to the original position. The same shift is also observed in YNi_2Al_3 [16,35] and $i7$ - PrNi_2Al_3 [17]. Refinement as orthorhombic trilling, as suggested by the *translationengleiche* symmetry reduction of index 3, is not necessary because the orthorhombic crystal system was found directly by the indexing routine.

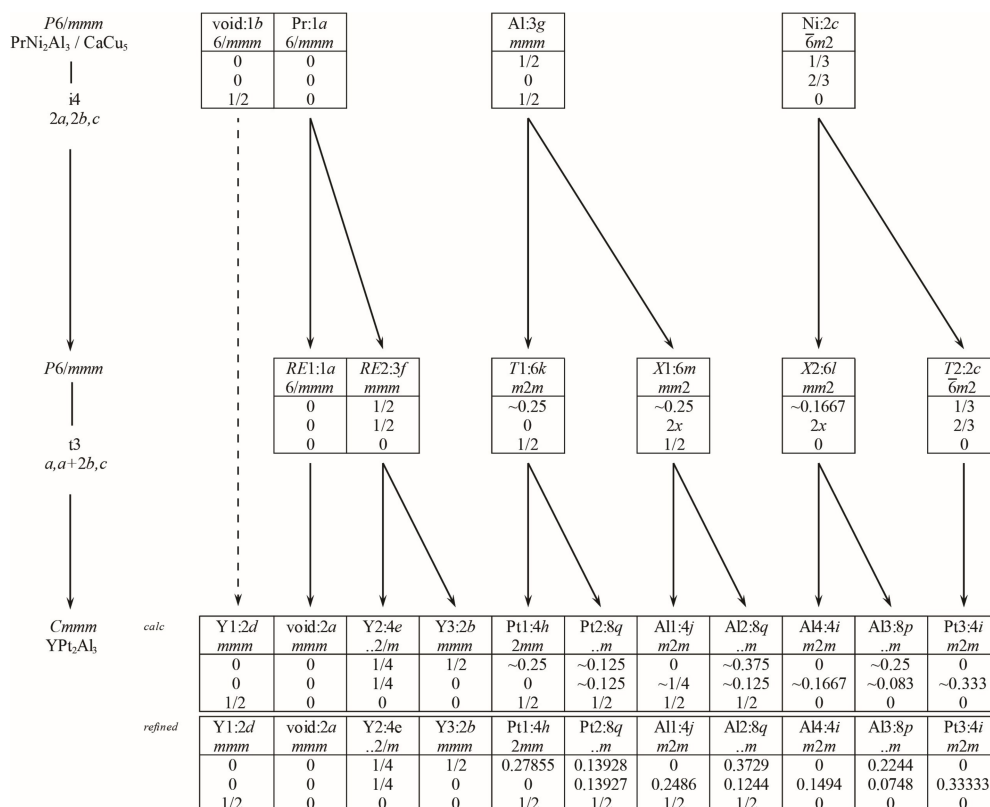


Figure 5. Group-subgroup scheme in the Bärnighausen formalism [36–39] for the structures of PrNi_2Al_3 and YPt_2Al_3 . The index for the isomorphic (i) and *translationengleiche* (t) symmetry reduction, the unit cell transformation, and the evolution of the atomic parameters are given.

3.3. Crystal Chemistry of $\text{Tm}_2\text{Pt}_3\text{Al}_4$ and $\text{Lu}_2\text{Pt}_3\text{Al}_4$

$\text{Tm}_2\text{Pt}_3\text{Al}_4$ and $\text{Lu}_2\text{Pt}_3\text{Al}_4$ crystallize in the orthorhombic crystal system with space group $Pnma$ ($oP36$, c^9) in the $\text{Ce}_2\text{Ir}_3\text{Sb}_4$ -type structure [26,27]. In the following paragraph, $\text{Lu}_2\text{Pt}_3\text{Al}_4$ will be used for the structure description. As in the REPt_2Al_3 series, the platinum and aluminum atoms form a network. Figure 6 depicts the extended unit cell along [010], and the polyanionic $[\text{Pt}_3\text{Al}_4]^{6-}$ network and the two different lutetium sites are highlighted. The heteroatomic Pt–Al distances span a larger range (246–269 pm) compared to YPt_2Al_3 ; however, Pt–Al bonding is still present. In contrast to YPt_2Al_3 , only additional Al–Al bonds can be found ranging from 278 to 300 pm. In the polyanion, no Pt–Pt bonds below 400 pm are found. The Al atoms form corrugated layers consisting of rectangles and hexagons in the boat conformation (Figure 7, top) that are capped by the Pt atoms (Figure 7, bottom).

The lutetium cations occupy two distinct crystallographic sites and are again found in the cavities of the polyanion. Lu1 is surrounded by 16 atoms in a four-fold-capped hexagonal prismatic environment ($\text{Lu1} @ [\text{Al}_6\text{Pt}_6 + \text{Al}_4]$; Figure 8, top), while Lu2 has a three-fold-capped pentagonal prismatic coordination sphere ($\text{Lu2} @ [\text{Al}_6\text{Pt}_4 + \text{Al}_2\text{Pt}]$; Figure 8, bottom). The Lu–Pt distances range from 299 to 310 pm, and the Lu–Al distances range from 327 to 347 pm. The Lu–Pt distances are in line with LuPtAl ; the Lu–Al contacts are significantly longer (Lu–Pt: 302–327 pm; Lu–Al: 284–301 pm) [30].

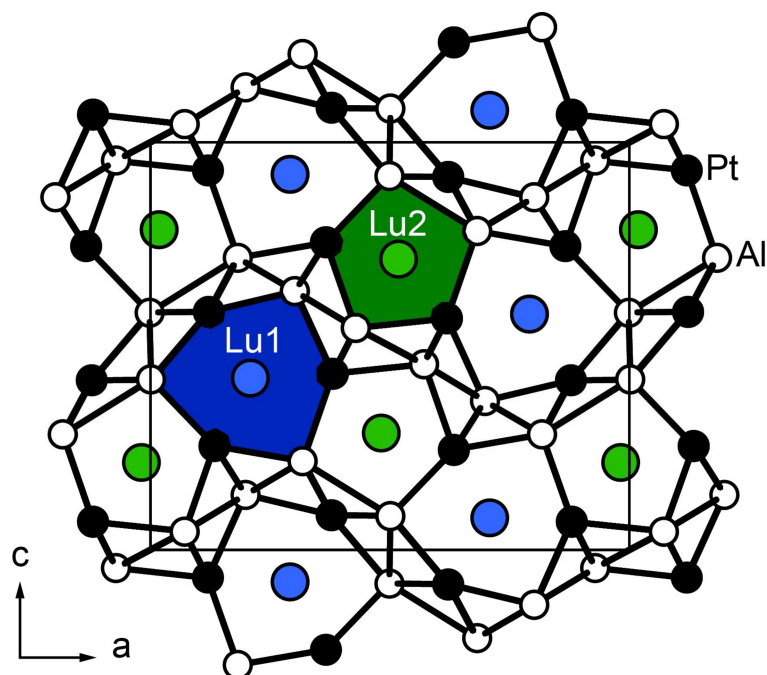


Figure 6. Extended crystal structure of $\text{Lu}_2\text{Pt}_3\text{Al}_4$ along [010]. Lutetium, platinum, and aluminum atoms are drawn as green/blue, black-filled, and open circles, respectively. The polyanionic $[\text{Pt}_3\text{Al}_4]^{4-}$ network and the two different coordination environments for the lutetium atoms are highlighted.

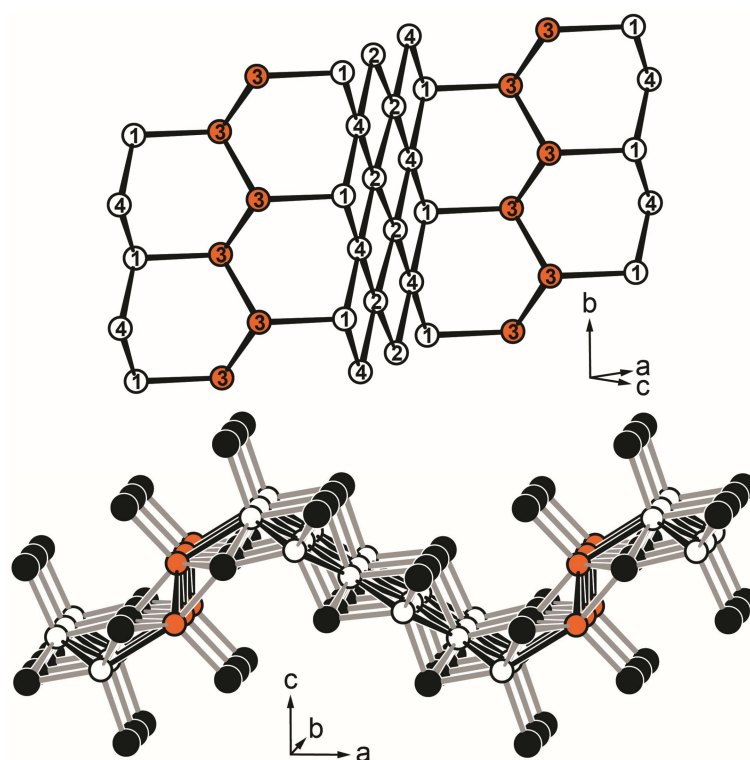


Figure 7. The Al arrangement in the crystal structure of $\text{Lu}_2\text{Pt}_3\text{Al}_4$ (top). The Pt atoms capping the layers are depicted in the bottom image. Platinum and aluminum atoms are drawn as black-filled and open circles, respectively. The Pt–Al bonds in the polyanionic $[\text{Pt}_3\text{Al}_4]^{4-}$ network are highlighted.

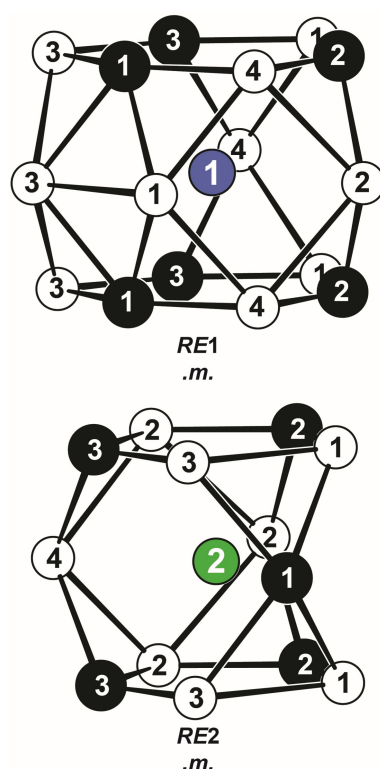


Figure 8. Coordination polyhedra surrounding the two crystallographically independent lutetium sites in $\text{Lu}_2\text{Pt}_3\text{Al}_4$. Lutetium, platinum, and aluminum atoms are drawn as green/blue, black-filled, and open circles, respectively. The local site symmetries are given.

3.4. Magnetic Properties

Magnetic susceptibility data has been obtained for the X-ray pure REPt_2Al_3 samples with $\text{RE} = \text{Y}$, Dy–Tm. The basic magnetic parameters that have been derived from these measurements are listed in Table 9. The temperature dependence of the magnetic susceptibility of the yttrium compound is depicted in Figure 9. YPt_2Al_3 is a *Pauli*-paramagnetic material with a room temperature susceptibility of $\chi = 1.85(1) \times 10^{-4} \text{ emu mol}^{-1}$. The weak upturn at lower temperature arises from small amounts of paramagnetic impurities. The present data clearly proves the absence of local moments on all constituent atoms. Thus, the magnetic properties of the remaining phases arise solely from the rare-earth elements.

The magnetic properties of DyPt_2Al_3 , HoPt_2Al_3 , ErPt_2Al_3 , and TmPt_2Al_3 have been depicted in Figures 10–13. The top panels always depict the susceptibility and inverse susceptibility data (χ and χ^{-1}). The effective magnetic moments have been obtained from fitting the χ^{-1} data using the Curie–Weiss law between 50 and 300 K. They were calculated from the Curie constant according to $\mu_{\text{eff}} = \sqrt{\frac{3k_{\text{B}}C}{N_{\text{A}}}}$ [40,41]. All rare-earth atoms are in the trivalent oxidation state; the effective magnetic moments compare well within the calculated moments, as stated in Table 9. The calculated moments are tabulated [40,41] or can be calculated according to $\mu_{\text{calc}} = g\sqrt{J(J+1)}$ with $g = 1 + \frac{J(J+1) + S(S+1) - L(L+1)}{2J(J+1)}$ [40,41].

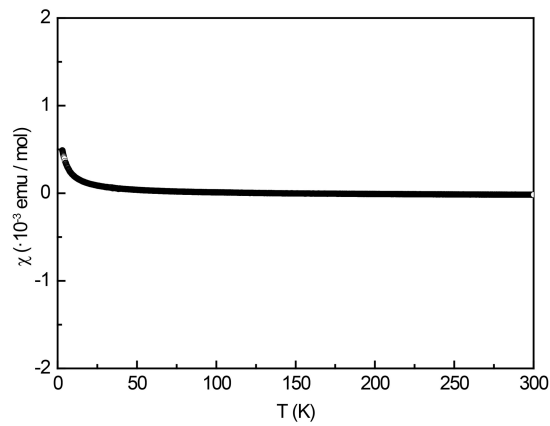


Figure 9. Temperature dependence of the magnetic susceptibility (data) of YPt_2Al_3 measured at 10 kOe.

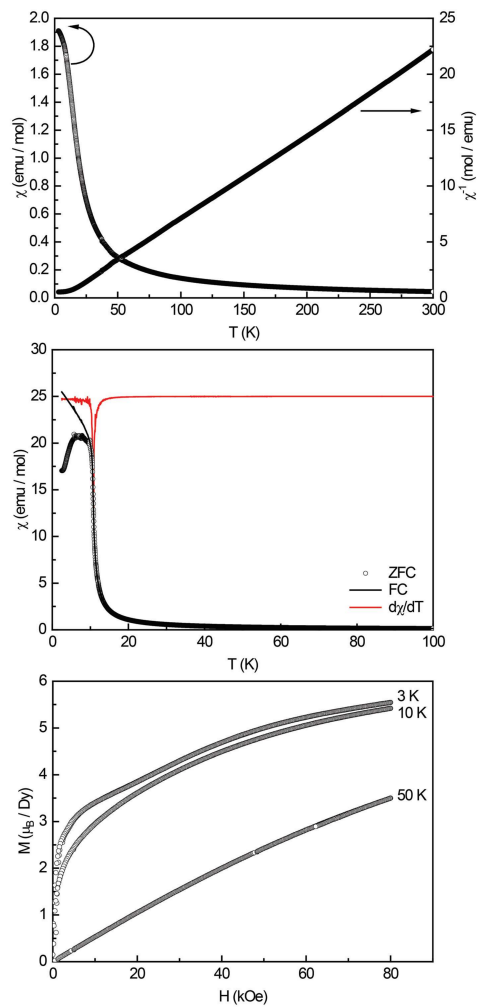


Figure 10. Magnetic properties of DyPt_2Al_3 : **(top)** temperature dependence of the magnetic susceptibility χ and its inverse χ^{-1} measured at 10 kOe; **(middle)** zero-field-cooled/field-cooled (ZFC/FC) data (100 Oe) and the $d\chi/dT$ derivative (red curve) of the FC curve; and **(bottom)** magnetization isotherms recorded at 3, 10, and 50 K.

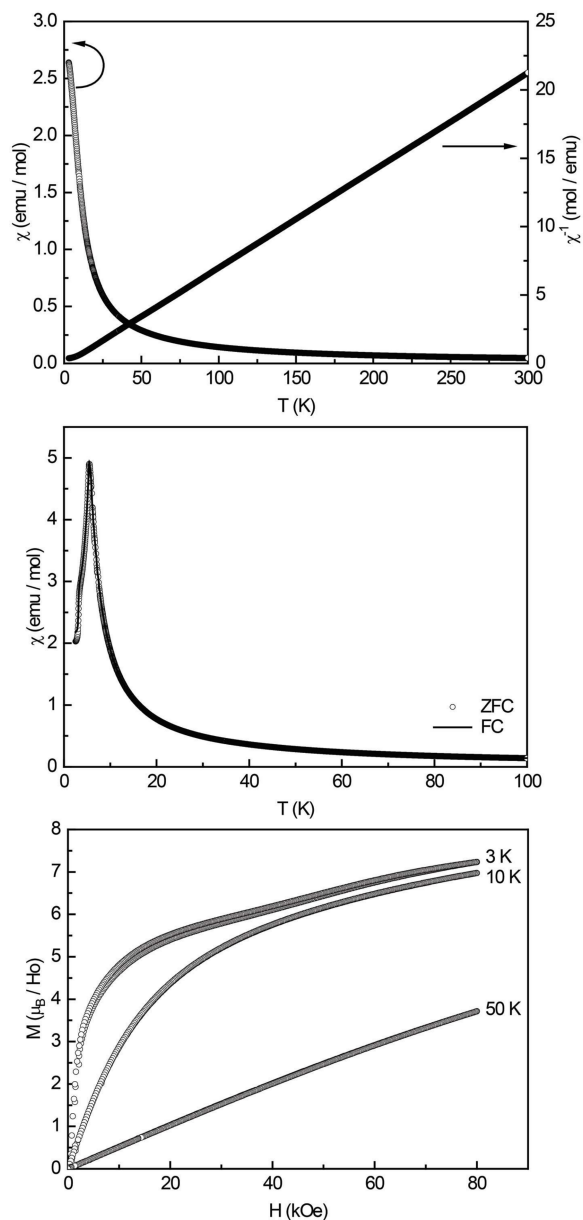


Figure 11. Magnetic properties of HoPt_2Al_3 : **(top)** temperature dependence of the magnetic susceptibility χ and its inverse χ^{-1} measured at 10 kOe; **(middle)** zero-field-cooled/field-cooled (ZFC/FC) data (100 Oe); and **(bottom)** magnetization isotherms recorded at 3, 10, and 50 K.

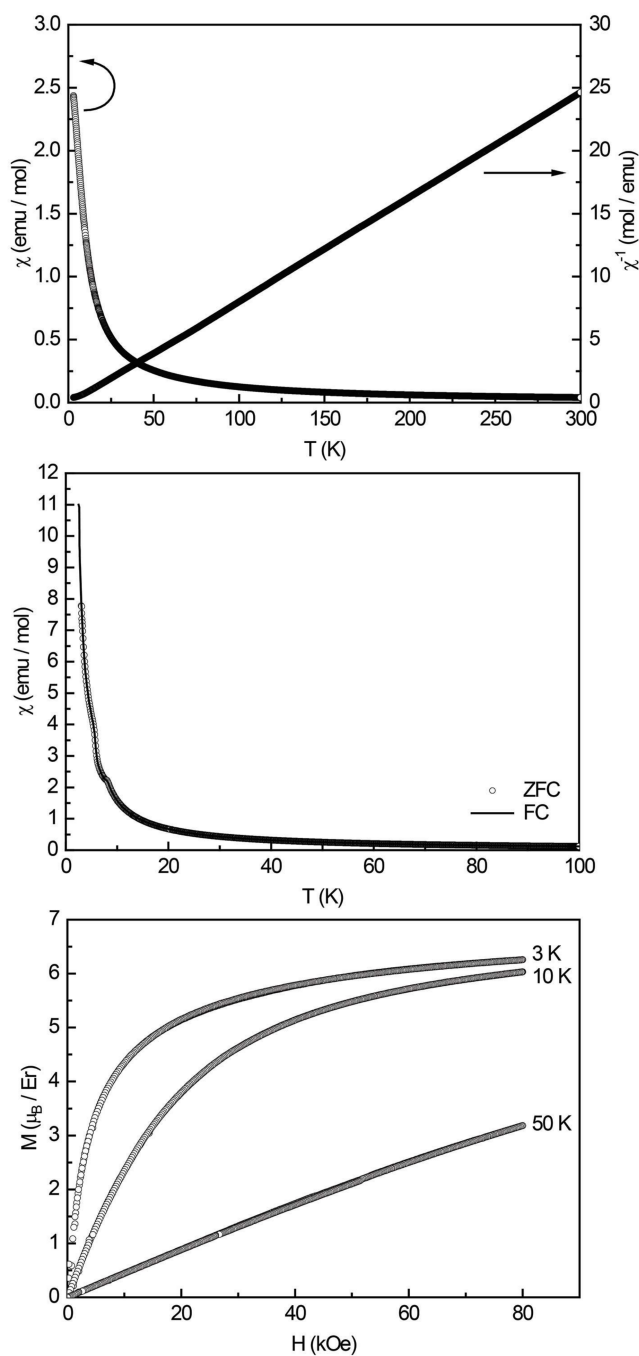


Figure 12. Magnetic properties of ErPt_2Al_3 : **(top)** temperature dependence of the magnetic susceptibility χ and its inverse χ^{-1} measured at 10 kOe; **(middle)** zero-field-cooled/field-cooled (ZFC/FC) data (100 Oe); and **(bottom)** magnetization isotherms recorded at 3, 10, and 50 K.

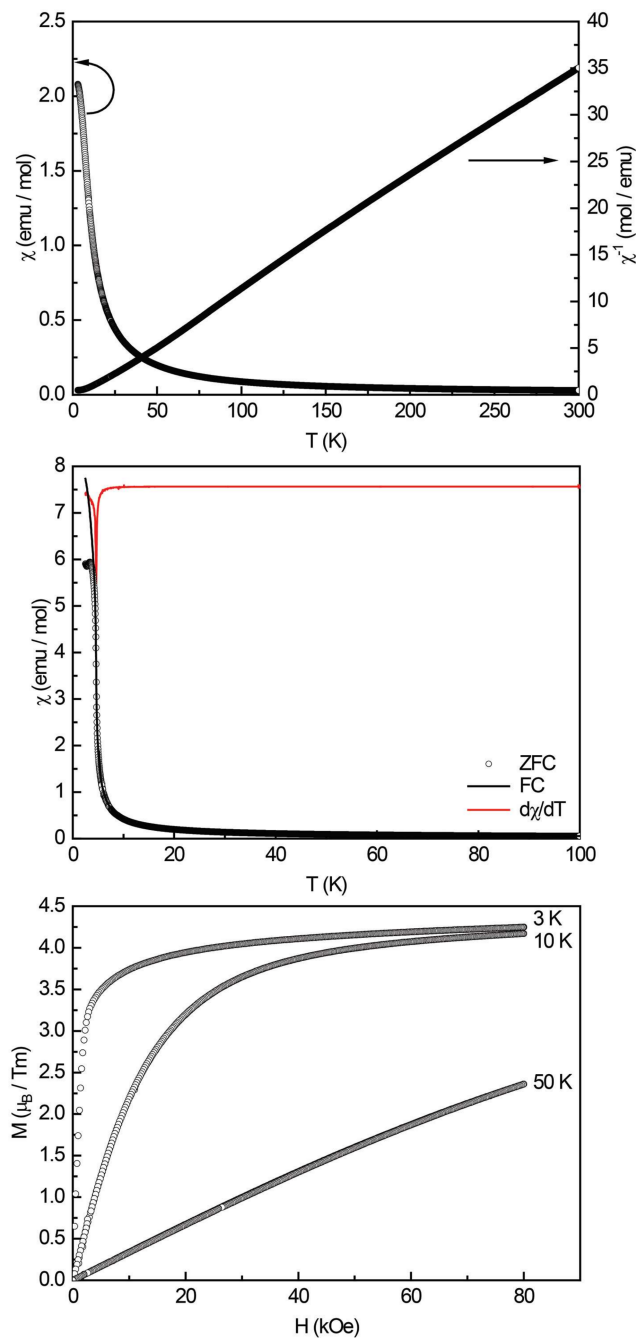


Figure 13. Magnetic properties of TmPt_2Al_3 : **(top)** temperature dependence of the magnetic susceptibility χ and its inverse χ^{-1} measured at 10 kOe; **(middle)** zero-field-cooled/field-cooled (ZFC/FC) data (100 Oe) and the $d\chi/dT$ derivative (red curve) of the FC curve; and **(bottom)** magnetization isotherms recorded at 3, 10, and 50 K.

Because a positive Weiss constant of θ_P is observed for the antiferromagnetically ordered compounds, the ordering phenomena could be a so-called Type-A antiferromagnetic ground state. In this ordered state, the intra-plane coupling is ferromagnetic while inter-plane coupling is antiferromagnetic [42]. From the zero-field-cooled/field-cooled (ZFC/FC) measurements depicted in the middle panels, it is evident that DyPt_2Al_3 and TmPt_2Al_3 exhibit ferromagnetic ordering at Curie temperatures of $T_C = 10.8(1)$ and $4.7(1)$ K due to the plateau-like susceptibility at low temperatures. ErPt_2Al_3 exhibits no magnetic ordering down to 2.5 K, while HoPt_2Al_3 finally orders

antiferromagnetically at $T_N = 5.5(1)$ K, characterized by decreasing susceptibility below the Néel temperature. The Curie temperatures were obtained from the derivatives $d\chi/dT$ of the field-cooled curves (depicted in red) by determination of the temperature at the minimum in the derivative curve. The bottom panels finally display the magnetization isotherms measured at 3, 10, and 50 K. The 3 K isotherms of DyPt_2Al_3 and TmPt_2Al_3 show a fast increase at low fields, in line with the ferromagnetic ground state. The 3 K isotherm of HoPt_2Al_3 displays a slightly delayed increase, suggesting a spin-reorientation, in line with a weak antiferromagnetic ground state. The 3 K isotherm of DyPt_2Al_3 displays small ‘wiggles’, suggesting trace impurities, which are hardly noticeable in the ZFC/FC measurements. In the 3 K isotherm of HoPt_2Al_3 , a small bifurcation is visible, also suggesting trace impurities, visible around 3 K in the ZFC/FC measurements. The isotherms at 50 K are all linear, in line with paramagnetic materials. The saturation magnetizations determined at 3 K and 80 kOe are all below the calculated values according to $g_J \times J$ (Table 9). The extracted values are, in all cases, lower than the expected moments, suggesting that the applied external field is not strong enough to achieve full parallel spin ordering.

3.5. X-ray Photoelectron Spectroscopy

The reported compounds were described by rare-earth cations located in the cavities of a polyanion. Hence, the rare-earth atoms transfer electron density to the framework. This is in line with the effective magnetic moments of the rare-earth cations, proving them to be formally in a trivalent oxidation state. When looking at the electronegativities χ of the constituting elements of the REPt_2Al_3 series, it is evident that platinum is by far the most electronegative element. According to the *Pauling* scale, the values are as follows: $\chi(\text{Y}) = 1.22$, $\chi(\text{Dy}) = 1.22$, $\chi(\text{Ho}) = 1.23$, $\chi(\text{Er}) = 1.24$, $\chi(\text{Tm}) = 1.25$, $\chi(\text{Pt}) = 2.28$, and $\chi(\text{Al}) = 1.61$ [30]. Because all reported compounds are of a metallic nature, a distinct ionic platinide character as found in A_2Pt ($\text{A} = \text{K}$ [43], Rb [43], Cs [43,44]) is highly unlikely, especially when considering the three-dimensional framework with strong covalent bonding character formed by Pt and Al. Therefore, XPS measurements were performed to investigate exemplarily the platinide character of YPt_2Al_3 along with the reference substances YPt_5Al_2 (*anti*- ZrNi_2Al_5 -type [45]), YPtAl (TiNiSi -type [31]), and elemental Pt.

The obtained binding energies are listed in Table 10. Figure 14 depicts an exemplary fitted spectrum of YPt_2Al_3 . As observed for $\text{Ba}_3\text{Pt}_4\text{Al}_4$ ($E_b(\text{Pt } 4f_{7/2}) = 70.9$ eV) [46], the binding energies of YPt_2Al_3 ($E_b(\text{Pt } 4f_{7/2}) = 70.4$ eV), YPt_5Al_2 ($E_b(\text{Pt } 4f_{7/2}) = 70.6$ eV), and YPtAl ($E_b(\text{Pt } 4f_{7/2}) = 70.2$ eV) are all shifted towards lower binding energies in comparison with elemental Pt ($E_b(\text{Pt } 4f_{7/2}) = 71.2$ eV). This can be explained by a higher electron density at the Pt atoms, in line with an electron transfer from the less electronegative Y and Al atoms. The existing literature [46] shows shifts of the Pt $4f_{7/2}$ signal towards higher binding energies for the binary phases PtAl and PtAl_2 (PtAl : 71.6, PtAl_2 : 72.1 eV), which can be explained by the bond formation between Pt and Al. In the ternary compounds, the additional electron transfer from the rare-earth atoms causes the lower binding energies and the ‘platinide’ character. While YPtAl and YPt_2Al_3 exhibit extensive Pt–Al bonding within the polyanion, only few heteroatomic Pt–Al bonds are observed in Pt-rich YPt_5Al_2 . Consequently, the spectra of YPt_5Al_2 show the smallest shift in comparison with elemental Pt. In YPtAl , an equal ratio of Pt and Al can be found in contrast with YPt_2Al_3 . In the latter compound, additional homoatomic bonding takes place; therefore, YPt_2Al_3 shows a smaller shift in the Pt $4f_{7/2}$ binding energies than YPtAl . As expected, Y is acting as electron donor, and therefore, the Y $3d_{5/2}$ signal is shifted by approximately 1 eV to higher binding energies (c.f. Table 10). However, all samples show a minor Y $3d_{5/2}$ component, that appears around 155.5 eV, in line with possible contaminations by traces of elemental yttrium.

Table 10. Fitted binding energies (in eV) determined by XPS of YPt_2Al_3 , YPt_5Al_2 , YPtAl , PrPtAl , and Pt and data from the literature. The determined uncertainty of binding energies in this work is ± 0.1 eV.

| Compound | Pt 4f _{7/2} | Al 2s | Y 3d _{5/2} | Lit. |
|-------------------------------------|----------------------|-------|---------------------|------|
| YPt_2Al_3 | 70.6 | 117.2 | 156.9 | * |
| YPt_5Al_2 | 70.9 | 117.8 | 157.0 | * |
| YPtAl | 70.4 | 116.7 | 156.6 | * |
| PrPtAl | 70.7 | ** | — | * |
| Pt | 71.4 | — | — | * |
| Pt | 71.2 | — | — | [46] |
| $\text{Ba}_3\text{Pt}_4\text{Al}_4$ | 70.9 | — | — | [46] |
| PtAl | 71.6 | — | — | [46] |
| PtAl_2 | 72.1 | — | — | [46] |

* This work. ** Signal invisible due to overlap with Pr 3d.

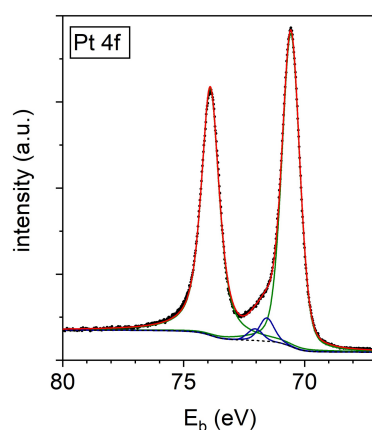


Figure 14. Fitted X-ray photoemission spectrum of Pt 4f in YPt_2Al_3 . The experimental data is shown as black squares, the Pt 4f components are depicted in green, the Al 2p lines in blue, and the envelope function in red. The background is depicted as a dashed line.

4. Conclusions

Attempts to synthesize the CaCu_5 -type related compounds REPt_2Al_3 with the late rare-earth elements Dy–Tm and Y led to the discovery of a new structure type, which was refined from single-crystal data obtained for YPt_2Al_3 . The structure crystallizes in the orthorhombic space group $Cmmm$ and can be derived from CaCu_5 by distortion and recoloring of the framework. Attempts to synthesize LuPt_2Al_3 led to the discovery of $\text{Lu}_2\text{Pt}_3\text{Al}_4$ ($\text{Ce}_2\text{Ir}_3\text{Sb}_4$ -type), which was also refined from single-crystal data. The REPt_2Al_3 compounds could be obtained in phase pure form for property investigations. While YPt_2Al_3 is *Pauli*-paramagnetic, DyPt_2Al_3 to TmPt_2Al_3 , in contrast, show paramagnetism in line with formal RE^{3+} cations, along with magnetic ordering for $\text{RE} = \text{Dy}$, Ho , and Tm at low temperatures. Via XPS investigations, the binding energies of the constituent elements were investigated and compared with the electronegativities. In comparison with reference substances, the expected charge transfer onto the Pt atoms within the polyanionic $[\text{Pt}_2\text{Al}_3]^{\delta-}$ network could be proven.

Acknowledgments: We thank Dipl.-Ing. Ute Ch. Rodewald for its collection of the single-crystal diffractometer data. The XPS facility has been co-funded by the Deutsche Forschungsgemeinschaft (INST 184/144-1 FUGG).

Author Contributions: Fabian Eustermann and Simon Gausebeck performed the synthesis and the powder diffraction experiments; Fabian Eustermann, Simon Gausebeck and Oliver Janka solved and refined the single crystal structures; Carsten Dosche and Mareike Haensch measured and analyzed the XPS spectra; Oliver Janka measured and analyzed the magnetic data. Carsten Dosche, Gunther Wittstock and Oliver Janka wrote the paper.

Conflicts of Interest: The authors declare no conflict of interest.

References

1. Dshemuchadse, J.; Steurer, W. *Intermetallics: Structures, Properties, and Statistics*; Union of Crystallography, Oxford University Press: Oxford, UK, 2016.
2. Pöttgen, R.; Johrendt, D. *Intermetallics—Synthesis, Structure, Function*; De Gruyter: Berlin, Germany; Boston, MA, USA, 2014.
3. Villars, P.; Cenzual, K. *Pearson's Crystal Data: Crystal Structure Database for Inorganic Compounds (on DVD)*; Villars, P., Cenzual, K., Eds.; ASM International®: Materials Park, OH, USA, Release 2017/2018.
4. Friauf, J.B. The crystal structures of two intermetallic compounds. *J. Am. Chem. Soc.* **1927**, *49*, 3107–3114. [[CrossRef](#)]
5. Lieser, K.H.; Witte, H. Untersuchungen in den ternären Systemen Magnesium-Kupfer-Zink, Magnesium-Nickel-Zink und Magnesium-Kupfer-Nickel. *Z. Metallkd.* **1952**, *43*, 396–401.
6. Johanssonm, C.H.; Linde, J.O. Röntgenographische Bestimmung der Atomanordnung in den Mischkristallreihen Au-Cu und Pd-Cu. *Annal. Physik* **1925**, *78*, 439–460. [[CrossRef](#)]
7. Nowotny, H.N. Die Kristallstrukturen von Ni₅Ce, Ni₅La, Ni₅Ca, Cu₅La, Cu₅Ca, Zn₅La, Zn₅Ca, Ni₂Ce, MgCe, MgLa und MgSr. *Z. Metallkd.* **1942**, *34*, 247–253.
8. Ban, Z.; Sikirica, M. The crystal structure of ternary silicides ThM₂Si₂ (M = Cr, Mn, Fe, Co, Ni and Cu). *Acta Crystallogr.* **1965**, *18*, 594–599. [[CrossRef](#)]
9. Markiv, V.Y.; Matushevskaya, N.F.; Rozum, S.N.; Kuz'ma, Y.B. Investigation of aluminum-rich alloys of the system Zr-Ni-Al. *Inorg. Mater.* **1966**, *2*, 1356–1359.
10. Gupta, S.; Suresh, K.G. Review on magnetic and related properties of RTX compounds. *J. Alloy Compd.* **2015**, *618*, 562–606. [[CrossRef](#)]
11. Pöttgen, R.; Chevalier, B. Cerium intermetallics with ZrNiAl-type structure—A review. *Z. Naturforsch. B* **2015**, *70*, 289–304. [[CrossRef](#)]
12. Pöttgen, R.; Janka, O.; Chevalier, B. Cerium intermetallics CeTX—Review III. *Z. Naturforsch. B* **2016**, *71*, 165–191. [[CrossRef](#)]
13. Janka, O.; Niehaus, O.; Pöttgen, R.; Chevalier, B. Cerium intermetallics with TiNiSi-type structure. *Z. Naturforsch. B* **2016**, *71*, 737–764. [[CrossRef](#)]
14. Kuz'ma, Y.B.; Krypyakevych, P.I.; Bilonizhko, N.S. Crystal structure of CeCo₃B₃ and analogous compounds. *Dopov. Akad. Nauk Ukr. RSR* **1969**, *A31*, 939–941.
15. Rykhal, R.M.; Zarechnyuk, O.S.; Kuten, J.I. Isothermal section at 800 °C for the praseodymium-nickel-aluminium ternary system in the range of 0–33.3 at.% of praseodymium. *Dopov. Akad. Nauk Ukr. RSR* **1978**, *A10*, 1136–1138.
16. Zarechnyuk, O.S.; Rykhal, R.M. Crystal Structure of the Compound YNi₂Al₃ and Related Phases. *Visn. Lviv. Derzh. Univ., Ser. Khim.* **1981**, *23*, 45–47.
17. Eustermann, F.; Hoffmann, R.-D.; Janka, O. Superstructure formation in PrNi₂Al₃ and ErPd₂Al₃. *Z. Kristallogr.* **2017**, *232*, 573–581. [[CrossRef](#)]
18. Blazina, Z.; Westwood, S.M. On the structural and magnetic properties of the CePt_{5-x}Al_x system. *J. Alloy Compd.* **1993**, *201*, 151–155. [[CrossRef](#)]
19. Pöttgen, R.; Gulden, T.; Simon, A. Miniaturisierte Lichtbogenapparat für den Laborbedarf. *GIT Labor-Fachz.* **1999**, *43*, 133–136.
20. Pöttgen, R.; Lang, A.; Hoffmann, R.-D.; Künnen, B.; Kotzyba, G.; Müllmann, R.; Mosel, B.D.; Rosenhahn, C. The stannides YbPtSn and Yb₂Pt₃Sn₅. *Z. Kristallogr.* **1999**, *214*, 143–150. [[CrossRef](#)]
21. Yvon, K.; Jeitschko, W.; Parthé, E. LAZY PULVERIX, a computer program, for calculating X-ray and neutron diffraction powder patterns. *J. Appl. Crystallogr.* **1977**, *10*, 73–74. [[CrossRef](#)]
22. Dectris. *Technical Specification and Operating Procedure Pilatus 100K-S Detector System, Version 1.7*; Dectris: Baden-Daettwil, Switzerland, 2011.
23. Palatinus, L.; Chapuis, G. SUPERFLIP—A computer program for the solution of crystal structures by charge flipping in arbitrary dimensions. *J. Appl. Crystallogr.* **2007**, *40*, 786–790. [[CrossRef](#)]
24. Petříček, V.; Dušek, M.; Palatinus, L. *Jana2006. The Crystallographic Computing System*; Institute of Physics: Praha, Czech Republic, 2006.
25. Petříček, V.; Dušek, M.; Palatinus, L. Crystallographic Computing System JANA2006: General features. *Z. Kristallogr.* **2014**, *229*, 345–352. [[CrossRef](#)]

26. Schäfer, K.; Hermes, W.; Rodewald, U.C.; Hoffmann, R.-D.; Pöttgen, R. Ternary Antimonides $RE_2Ir_3Sb_4$ ($RE = La, Ce, Pr, Nd$). *Z. Naturforsch. B* **2011**, *66*, 777–783. [\[CrossRef\]](#)
27. Cardoso-Gil, R.; Caroca-Canales, N.; Budnyk, S.; Schnelle, W. Crystal structure, chemical bonding and magnetic properties of the new antimonides $Ce_2Ir_3Sb_4$, $La_2Ir_3Sb_4$, and $Ce_2Rh_3Sb_4$. *Z. Kristallogr.* **2011**, *226*, 657–666. [\[CrossRef\]](#)
28. Shannon, R.D. Revised effective ionic radii and systematic studies of interatomic distances in halides and chalcogenides. *Acta Crystallogr.* **1976**, *A32*, 751. [\[CrossRef\]](#)
29. Emsley, J. *The Elements*; Clarendon Press-Oxford University Press: Oxford, UK; New York, NY, USA, 1998.
30. Dwight, A.E. Crystal structure of equiatomic ternary compounds: Lanthanide-transition metal aluminides. *J. Less-Common Met.* **1984**, *102*, L9–L13. [\[CrossRef\]](#)
31. Thiede, V.M.T.; Fehrmann, B.; Jeitschko, W. Ternary Rare Earth Metal Palladium and Platinum Aluminides $R_4Pd_9Al_{24}$ and $R_4Pt_9Al_{24}$. *Z. Anorg. Allg. Chem.* **1999**, *625*, 1417–1425. [\[CrossRef\]](#)
32. Hull, A.W. The positions of atoms in metals. *Proc. Am. Inst. Electr. Eng.* **1919**, *38*, 1445–1466. [\[CrossRef\]](#)
33. Hull, A.W. A New Method of X-Ray Crystal Analysis. *Phys. Rev.* **1917**, *10*, 661–696. [\[CrossRef\]](#)
34. Morozkin, A.V.; Knotko, A.V.; Yapaskurt, V.O.; Yuan, F.; Mozharivskyj, Y.; Nirmala, R. New orthorhombic derivative of $CaCu_5$ -type structure: RNi_4Si compounds ($R = Y, La, Ce, Sm, Gd-Ho$), crystal structure and some magnetic properties. *J. Solid State Chem.* **2013**, *208*, 9–13. [\[CrossRef\]](#)
35. Pöttgen, R. Coloring, Distortions, and Puckering in Selected Intermetallic Structures from the Perspective of Group-Subgroup Relations. *Z. Anorg. Allg. Chem.* **2014**, *640*, 869–891. [\[CrossRef\]](#)
36. Bärnighausen, H. Group-Subgroup Relations between Space Groups: A Useful Tool in Crystal Chemistry. *Commun. Math. Chem.* **1980**, *9*, 139–175.
37. Bärnighausen, H.; Müller, U. *Symmetriebeziehungen Zwischen den Raumgruppen als Hilfsmittel zur Straffen Darstellung von Strukturzusammenhängen in der Kristallchemie*; Universität Karlsruhe und Universität-Gh: Kassel, Germany, 1996.
38. Müller, U. Kristallographische Gruppe-Untergruppe-Beziehungen und ihre Anwendung in der Kristallchemie. *Z. Anorg. Allg. Chem.* **2004**, *630*, 1519–1537. [\[CrossRef\]](#)
39. Müller, U. *Symmetry Relationships between Crystal Structures*; Oxford University Press: New York, NY, USA, 2013.
40. Lueken, H. *Magnetochemie*; B.G. Teubner: Stuttgart/Leipzig, Germany, 1999.
41. Cheetham, A.K.; Day, P. *Solid State Chemistry Techniques*; Oxford University Press: New York, NY, USA, 1991.
42. Wollan, E.O.; Koehler, W.C. Neutron Diffraction Study of the Magnetic Properties of the Series of Perovskite-Type Compounds $[(1-x)La_xCa]MnO_3$. *Phys. Rev.* **1955**, *100*, 545–563. [\[CrossRef\]](#)
43. Karpov, A.; Jansen, M. A New Family of Binary Layered Compounds of Platinum with Alkali Metals ($A = K, Rb, Cs$). *Z. Anorg. Allg. Chem.* **2006**, *632*, 84–90. [\[CrossRef\]](#)
44. Karpov, A.; Nuss, J.; Wedig, U.; Jansen, M. Cs_2Pt : A Platinide(-II) Exhibiting Complete Charge Separation. *Angew. Chem. Int. Ed.* **2003**, *42*, 4818–4821. [\[CrossRef\]](#) [\[PubMed\]](#)
45. Benndorf, C.; Stegemann, F.; Eckert, H.; Janka, O. New transition metal-rich rare-earth palladium/platinum aluminides with RE_2Al_2 composition: Structure, magnetism and ^{27}Al NMR spectroscopy. *Z. Naturforsch. B* **2015**, *70*, 101–110.
46. Stegemann, F.; Benndorf, C.; Bartsch, T.; Touzani, R.S.; Bartsch, M.; Zacharias, H.; Fokwa, B.P.T.; Eckert, H.; Janka, O. $Ba_3Pt_4Al_4$ —Structure, Properties, and Theoretical and NMR Spectroscopic Investigations of a Complex Platinide Featuring Heterocubane $[Pt_4Al_4]$ Units. *Inorg. Chem.* **2015**, *54*, 10785–10793. [\[CrossRef\]](#) [\[PubMed\]](#)

